SIAM J. Applied Dynamical Systems
Vol. 10, No. 4, pp. 1344–1362


# 2D Phase Diagram for Minimizers of a Cahn–Hilliard Functional with Long-Range Interactions*

Rustum Choksi†, Mirjana Maras‡, and J. F. Williams‡

**Abstract.** This paper presents a two-dimensional investigation of the phase diagram for global minimizers to a *Cahn–Hilliard functional with long-range interactions*. Based upon the $H^{-1}$ gradient flow, we introduce a hybrid numerical method to navigate through the complex energy landscape and access an *accurate* depiction of the ground state of the functional. We use this method to numerically compute the phase diagram in a (finite) neighborhood of the order-disorder transition. We demonstrate a remarkably strong agreement with the standard asymptotic estimates for stability regions based upon a small parameter measuring perturbation from the order-disorder transition curve.

**Key words.** simulation of the phase diagram, long-range interactions, Cahn–Hilliard equation, spectral weighting

**AMS subject classifications.** 49M30, 49S05

**DOI.** 10.1137/100784497

## 1. Introduction.

In this article, we numerically and asymptotically address the phase diagram with respect to the parameters $\gamma$ and $m$ for the following mass-constrained variational problem: For $\gamma > 0$ and $m \in (-1, 1)$, minimize

$$\int_\Omega \left( \frac{1}{\gamma^2} \frac{|\nabla u|^2}{2} + \frac{(1-u^2)^2}{4} \right) dx + \int_\Omega \int_\Omega G(x,y)\,(u(x)-m)\,(u(y)-m)\,dx\,dy \tag{1.1}$$

over all $u$ with $\fint_\Omega u\,dx = m$. Here $G$ denotes the Green's function of $-\triangle$ on a cubic domain $\Omega := [0, L]^n \subset \mathbb{R}^n$ with periodic boundary conditions. We refer to functional (1.1) as a Cahn–Hilliard functional (cf. [5]) with long-range interactions.[1] It may simply be viewed as a mathematical paradigm for *energy-driven pattern formation induced by competing short- and long-range interactions*: Minimization of the first two terms (short-range) leads to domains of pure phases of $u = \pm 1$ with minimal transition regions, whereas the third (long-range) term induces oscillations between the phases according to the set volume fraction $m$. On a sufficiently large domain $\Omega$, the competition of the two leads to pattern formation on an

*Received by the editors February 1, 2010; accepted for publication (in revised form) by B. Sandstede June 6, 2011; published electronically November 8, 2011. This research was partially supported by the NSERC (Canada) Discovery Grants program.
http://www.siam.org/journals/siads/10-4/78449.html
†Department of Mathematics, McGill University, Montreal, QC H3A 2K6, Canada (rchoksi@math.mcgill.ca).
‡Department of Mathematics, Simon Fraser University, Burnaby, BC V5A 1S6, Canada (mmaras@sfu.ca, jfw@math.sfu.ca).

[1] This functional is also commonly referred as a *Ginzburg–Landau* functional with *competing or Coulomb-type* interactions [35, 24], or because of its relation to self-assembly of diblock copolymers, the *Ohta–Kawasaki* functional [29], or simply as *the diblock copolymer problem* [33]. Our reference and labeling of *Cahn–Hilliard* is primarily due to tradition in the mathematical phase transitions community.

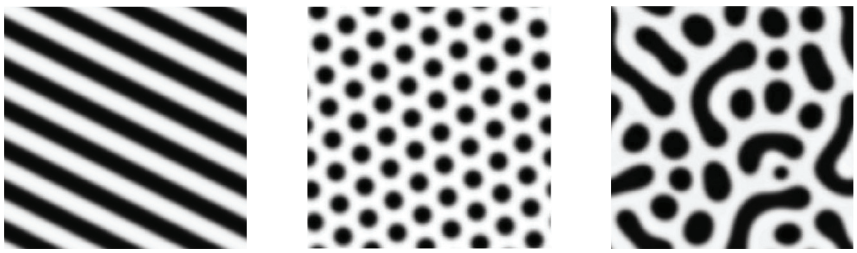

**Figure 1.** *Typical long-time solutions to (1.2) with $\gamma = 10$. Left: Lamellae, $m = 0$. This is a global minimizing state. Center: Hexagonally packed spots, $m = .3$. This is a global minimizing state. Right: A mixed state, $m = .4$. This is a typical metastable solution. All figures were computed on a domain of size $4\pi \times 4\pi$. Here and in the following figures, $u = 1$ is represented in black and $u = -1$ in white.*

intrinsic scale which depends entirely on $\gamma$. Throughout this article we always choose the physical domain $\Omega$ to be of size[2] much larger than this intrinsic scale (cf. Figure 1).

A tool for our computations is the $H^{-1}$ gradient flow (cf. [10]) for $\bar{u} := u - m$ which takes the form

$$\frac{\partial \bar{u}}{\partial t} = -\frac{1}{\gamma^2} \triangle^2 \bar{u} + \triangle \left( \bar{u}^3 + 3m\bar{u}^2 - (1 - 3m^2)\bar{u} \right) - \bar{u}, \tag{1.2}$$

with periodic boundary conditions. It is important to note here that we compute the gradient with respect to $H^{-1}$, a nonlocal metric. Hence the presence of the *nonlocal* term in the functional (1.1) simply gives rise to a *local* perturbation[3] of the standard Cahn–Hilliard equation. However, it significantly changes its behavior, making it in some ways a hybrid of the Swift–Hohenberg equation [40, 13] and the standard Cahn–Hilliard equation.

Whilst the functional (1.1) is mathematically interesting on its own, we were drawn to it because of its connection with self-assembly of diblock copolymers: the functional is a rescaled version of a functional introduced by Ohta and Kawasaki (see [29, 28, 2]). Melts of diblock copolymer display a rich class of self-assembly nanostructures from lamellae, spheres, and cylindrical tubes to double gyroids and other more complex structures (see, for example, [3, 17]). Moreover, the usefulness of block copolymer melts is exactly this remarkable ability for self-assembly into particular geometries. For example, this property can be exploited to create materials with *designer* mechanical, optical, and magnetic properties [3]. Therefore from a theoretical point of view, one of the main challenges is to predict the phase geometry/morphology for a given set of material parameters, that is, the creation of a phase diagram. As was explained in [10], the parameter $\gamma$ plays the role of the product $\chi N$, where $\chi$ denotes the Flory–Huggins interaction parameter and $N$ denotes the index of polymerization (cf. [16]).

The state of the art for predicting the phase diagram (in $\chi N$ vs. $m$ space) is via the self-consistent mean field theory (SCFT) [23, 16]. While the simple functional (1.1) can be connected with the SCFT via approximations (cf. [11]) with increasing validity close to the

[2]Since we do work on a finite domain (albeit sufficiently large), the choice of the exact domain size can still have an effect on the minimizing geometry; see section 4.4.

[3]Note that the gradient of the nonlocal term with respect to $L^2$ would be $(-\triangle)^{-1}(\bar{u})$, and working in $H^{-1}$ has the effect of introducing an additional $(-\triangle)$.

order-disorder transition (ODT), it is generally regarded as the basis of a qualitative theory, and one might question its usefulness with regard to predicting self-assembly structures for given material parameters. Preliminary numerical experiments [41, 10, 42] indicate that all the phases (including double gyroids and perforated lamellae), some of which had been predicted using the SCFT [23] and all of which have been observed for polystyrene-isoprene [17], can be simulated as minimizers of (1.1) starting from random initial conditions. This begs the question as to the extent to which a phase diagram via (1.1) can be compared with those of experimental observations and SCFT calculations, at least close to the ODT.

A thorough numerical phase diagram for (1.1) with $n = 3$ (three dimensions) is by no means an easy task. In addition to numerical complications associated with the stiff PDE (1.2) and the necessary small time steps and large spatial grids, the energy landscape of (1.1) is highly nonconvex, with multitudes of local minimizers and metastable states about which the gradient flow dynamics are very slow. Many of the the simulations we presented in [10] were not simply the final steady states for simulations of (1.2) with random initial conditions. Rather, one tended to get stuck in metastable states and some procedure for *exiting* these metastable states in order to flow to *lower* energy states was crucial. Such procedures are often loosely dubbed *simulated annealing*. The present article may be viewed as a *test case* for the three-dimensional (3D) phase diagram. The two-dimensional (2D) situation is greatly simplified, as the range of possible minimizers is both drastically reduced and, in fact, well accepted to involve only basic structures (cf. Remark 1.1): (i) disordered, i.e., minimizers of (1.1) are simply the uniform state $u \equiv m$; (ii) lamellar, i.e., minimizers of (1.1) have a one-dimensional (1D) structure; and (iii) spots, i.e., minimizers of (1.1) are a periodic array of (approximate) circles arranged on either a hexagonal or rectangular lattice (in what follows, all spot solutions are hexagonally packed unless otherwise indicated). Examples of the latter two cases and a metastable mixed state are presented in Figure 1. As is well known in the pattern formation literature, these standard solutions are in some sense enforced by the periodic boundary conditions, and predictions for their global and local stability can readily be found via asymptotic perturbation analysis close to the ODT of the linearized PDE (1.2). Thus the 2D situation presents an excellent *test case* to derive and test a numerical algorithm to *access* the ground state of (1.1), in particular a method which can go "below" metastable or local minimizing states and yield a lowest energy state which strongly resembles the ideal patterns (straight lamellar and hexagonally packed spots). To this end we do the following:

(i) We present a hybrid numerical method to address the complex metastability issues and provide access to the ground state of (1.1).

(ii) We record the results of this method over a vast sample of parameter space, extending well above the ODT.

(iii) We demonstrate that not only do standard asymptotic arguments predict the collection of possible phase geometries but there is a surprisingly strong agreement with respect to the *phase boundaries* suggesting that for the purposes of describing the basic geometric morphology of the ground state of (1.1), the linear behavior of (1.2) gives very accurate predictions in a (finite) neighborhood of the ODT. As we discuss in section 5, this unusual agreement is, in part, a consequence of the long-range interactions in (1.1) which favor a uniform state—exactly the asymptotic ansatz.

We are not aware of any other systematic study of global minimizers for similar models with

two parameters in two or more dimensions. The results presented in (i)–(iii) are particularly important with regard to a 3D study wherein the set of possible candidates for minimizers (global and local) is far more complex and in fact unknown. In fact an interesting question arises as to whether or not 3D asymptotic analysis can at least predict all the possible geometries of experimentally observed phases (cf. [17]). This would be rather telling given the simplicity and genericness of the linearization (2.1)—for example, it is almost identical to that of the Swift–Hohenberg equation.

We conclude by noting that the novelty of our 2D work lies in the focus on the energy and assessing its lowest state. The simple patterns involved here and transitions from one state to another across parameter space occur in many PDE models for pattern formation, some of which, like this one, are variational (cf. [30, 19, 26, 27, 2]). The bulk of these studies are based upon final time solutions of the PDE (for variational problems, critical points of the energy) and as such focus on *local* arguments. For instance, there is considerable interest in *localized* solutions to the Swift–Hohenberg equation and other similar equations in dimensions 1, 2, and 3—see, for example, [40, 13, 4, 37, 21, 30, 26, 27, 19, 32, 14] and the references therein.[4] Thus from the point of view of (local) asymptotic analysis and 2D simulations of a PDE which result in spots or stripes, there is nothing new here. Our focus is on the phase diagram, that is, global minimizers associated with the two-parameter, highly nonconvex energy landscape of the general functional (1.1).

*Remark* 1.1 (global minimizers/ground states). While existence of a global minimizer of (1.1) follows immediately from the direct method in the calculus of variations, even in two dimensions there are very few results pertaining to its structure. We refer the reader to [7, 25, 38, 1, 36] for partial results. Our simulations show level sets of (diffuse) phase boundaries which strongly resemble curves of constant curvature (lines and circles). This is also the case with 3D simulations and constant mean curvature surfaces. However, on a finite torus, the combination of long-range and boundary effects will dictate that phase boundaries of global and local minimizers will *not*, in general, have constant mean curvature (see [24, 12, 34]). At least for global minimizers, this perturbation from constant mean curvature seems to be very small (too small for numerical detection), and a rigorous attempt to address this was made in [9]. Thus one should keep in mind that our claimed depictions of the ground state are all modulo this caveat.

## 2. Asymptotic results.

Here we document the results of a asymptotic analysis for the linearization of (1.2) about $\bar{u} \equiv 0$:

$$v_t = \mathcal{L}v \equiv -\frac{1}{\gamma^2}\Delta^2 v - (1 - 3m^2)\Delta v - v. \tag{2.1}$$

Note that the linearization (2.1) is very similar to that of the Swift–Hohenberg equation for which similar asymptotic descriptions exist (see, for example, [5] and the references therein). However, for completeness we sketch the details in Appendix A. The ODT curve, determined

[4] In [31] periodic solutions to the Swift–Hohenberg equation are analyzed in one dimension with both the detuning parameter $\alpha$ and the imposed fundamental period length as parameters. For our problem, the period length is determined by the minimization procedure, and not solely by a parameter.

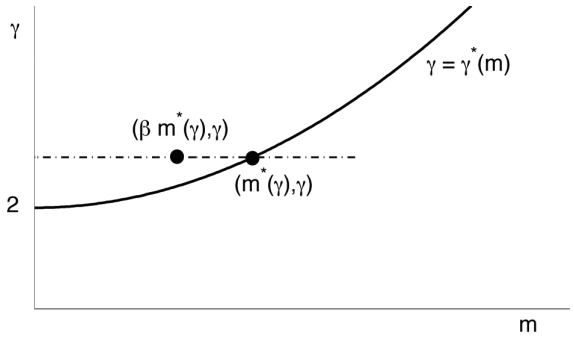


**Figure 2.** *Asymptotic coordinates. We identify points in the plane via* $(\beta m^*(\gamma), \gamma)$*, where* $m^*(\gamma) \ll 1$ *as* $\gamma \downarrow 2$.

by the condition that the maximum of the real part of the eigenvalues of $\mathcal{L}$ be 0, is given by

$$\gamma^* = \frac{2}{1-3m^2} \qquad \text{or} \qquad m^* = \sqrt{\frac{\gamma-2}{3\gamma}};$$

i.e., at fixed $\gamma$, $\bar{u} = 0$ is linearly stable for $m > m^*(\gamma)$ and unstable for $m < m^*(\gamma)$. For $\beta > 0$, we set $m = \beta m^*(\gamma)$ and identify points in the plane via $(m, \gamma)$, where $m^*(\gamma) \ll 1$ as $\gamma \downarrow 2$ (see Figure 2). Another way of saying this is that we consider the asymptotics as $(m, \gamma)$ approaches the point $(0, 2)$ along curves of the form $\gamma = \frac{2}{1-3\ m^2/\beta^2}$. Standard perturbation arguments (cf. Appendix A) result in the following three regions of linear stability:

$$\begin{cases} 0 \le \beta < \frac{1}{\sqrt{5}} & \text{lamellae,} \\ \frac{1}{\sqrt{17}} < \beta < \frac{\sqrt{5}}{2} & \text{hexagonally packed circular spots,} \\ \beta > 1 & \text{uniform (disorder),} \end{cases} \tag{2.2}$$

and the following three regions of global stability:

$$\begin{cases} 0 \le \beta < \frac{1}{29}\sqrt{551 - 174\sqrt{6}} & \text{lamellae,} \\ \frac{1}{29}\sqrt{551 - 174\sqrt{6}} < \beta < 3\sqrt{\frac{5}{37}} & \text{hexagonally packed circular spots,} \\ \beta > 3\sqrt{\frac{5}{37}} & \text{uniform (disorder).} \end{cases} \tag{2.3}$$

Figure 3 shows the asymptotic linear stability and global stability diagrams.

**3. Numerical simulations.** In this section we present the results of our numerical experiments and compare them with the asymptotic predictions of the previous section in regimes where they may present some validity. Our numerical method will be described in some detail in section 4. It is a hybrid method which not only integrates the PDE (1.2) but also involves an interplay with the energy (1.1) through certain methods of *simulated annealing*. For most values of the parameters $(m, \gamma)$, we believe that this method terminates in a depiction of the ground state of (1.1), at the very least from the point of its inherent structure (geometry and symmetry). Of course we have no proof of this statement (see Remark 1.1). We sampled the

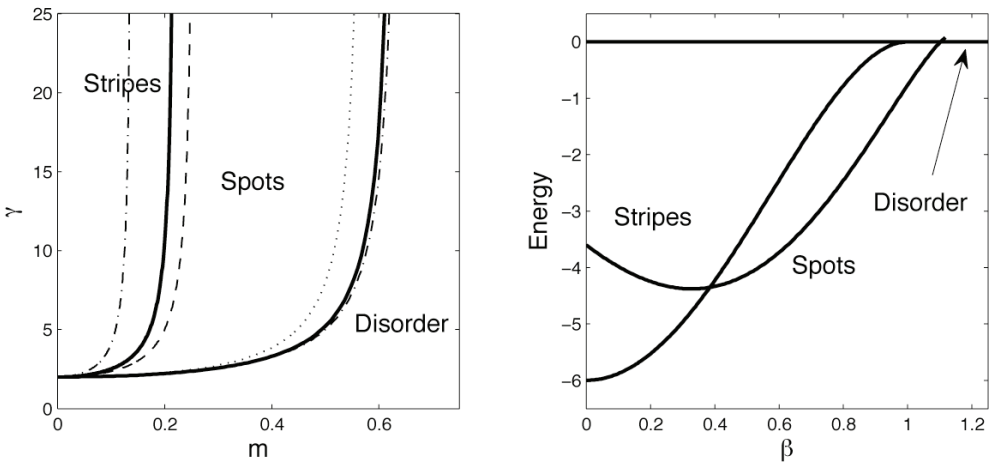


**Figure 3.** *Asymptotic results. Stability diagram of stationary solutions (left). Solid lines represent the global stability boundaries* (2.3) *and dashed lines are the linear stability boundaries* (2.2)*. Lamellae are globally stable between $m = 0$ and the first solid line and linearly stable until the dashed line. Spots are globally stable between the solid lines and linearly stable between the dash-dotted lines. The dotted line denotes the linear stability transition of the constant state. Energy* (A.4) *for steady solutions of* (A.3) *(right).*

parameter plane by taking a sequence of randomly chosen points $(m_i, \gamma_i) \in [0,1] \times [2,25]$ and implemented our method for each such $(m_i, \gamma_i)$ with $\bar{u}(x_i, y_j, t = 0) \in (-1, 1)$ randomly chosen from a uniform distribution. Once a sequence of more than 500 runs was complete, an edge detection algorithm was used to place additional points near the interfaces between regions where $\bar{u} = 0$, hex spots and lamellae being stable. For all runs we computed the energy (1.1) at each time step, making sure that the final presented state had the least energy over the course of the entire run.

**3.1. Results of numerical simulations.** Our numerical experiments confirm the asymptotic description of the stability curves and the solution structure in the limit $\gamma \downarrow 2$, $m^*(\gamma) \downarrow 0$. In Figure 4 we present the numerically computed bifurcation diagram with the asymptotic stability curves overlaid. Here $\times, \circ$, and $\diamond$ indicate stripes, hexagonally packed spots, and the disordered state, respectively. The solid lines mark the global stability curves and the dashed lines outline the linear stability regimes. Figure 4(top) displays a detailed examination of the phase diagram for $2 \leq \gamma \leq 5$ and demonstrates a remarkable agreement between numerics and asymptotics; for example, almost no runs converged to a state outside of its asymptotic region of global stability.

Figure 4(bottom) has $2 \leq \gamma \leq 25$, and the asymptotic estimates are now only in qualitative agreement as $\gamma$ increases. Limited additional runs up to $\gamma = 100$ were also performed and still show qualitative agreement with asymptotics in that no new phases were seen and the ordering of stripes, spots, and the homogeneous state occurs for increasing $m$. Unfortunately, the stability region of the PDE time-stepping routine quickly decreases with increasing $\gamma$ and the time scale of the PDE evolution slows down, making the runs with very large $\gamma$ increase in cost faster than $\gamma^2$ and hence be very computationally expensive. For increasing $\gamma$ we find that the stripe/spot transition is much better approximated by the asymptotics than the

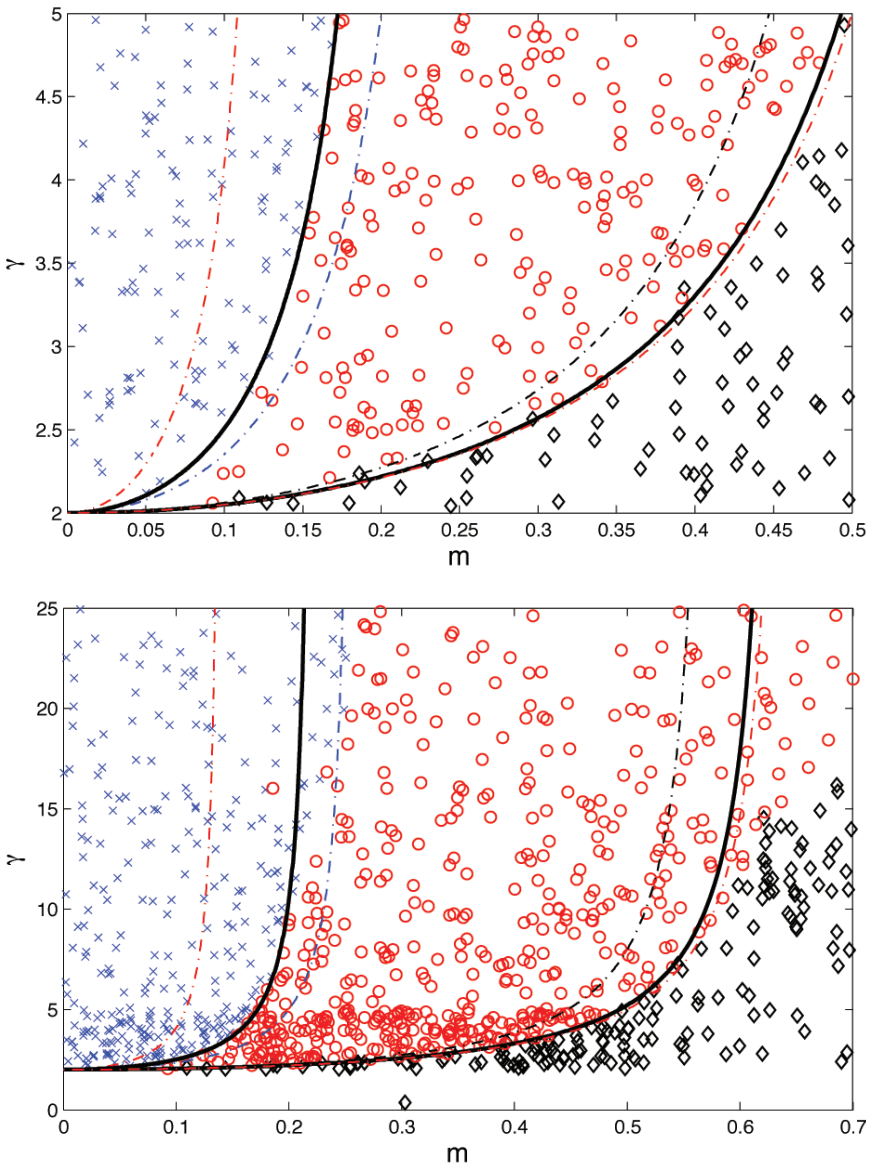


**Figure 4.** *Numerically computed phase diagram. (Bottom) Complete diagram. (Top) Detail for $\gamma$ close to 2. Blue crosses: Lamellae. Red circles: Hexagonally packed spots. Black diamonds: disorder. The red dashed-dotted lines mark the linear stability boundary of spots, the blue dashed-dotted line marks the linear stability boundary of lamellae, the black dashed-dotted line marks the linear stability boundary of the disordered sate, and the solid black lines mark the global stability regions of lamellae and spots, respectively.*

spot/homogeneous transition. That is, for increasing $\gamma$ there is an ever wider region where spots are globally stable but the homogeneous state is linearly stable.

Continuation in $m$ of spots and stripes was also performed for $\gamma = 2.001$, 2.01, 2.1, 2.25, 2.5, 3, 3.5, 5, 10, and 20. Comparing the energies of the different phases allows us to identify the global minimizer directly. Figure 5 shows that the agreement with the PDE-

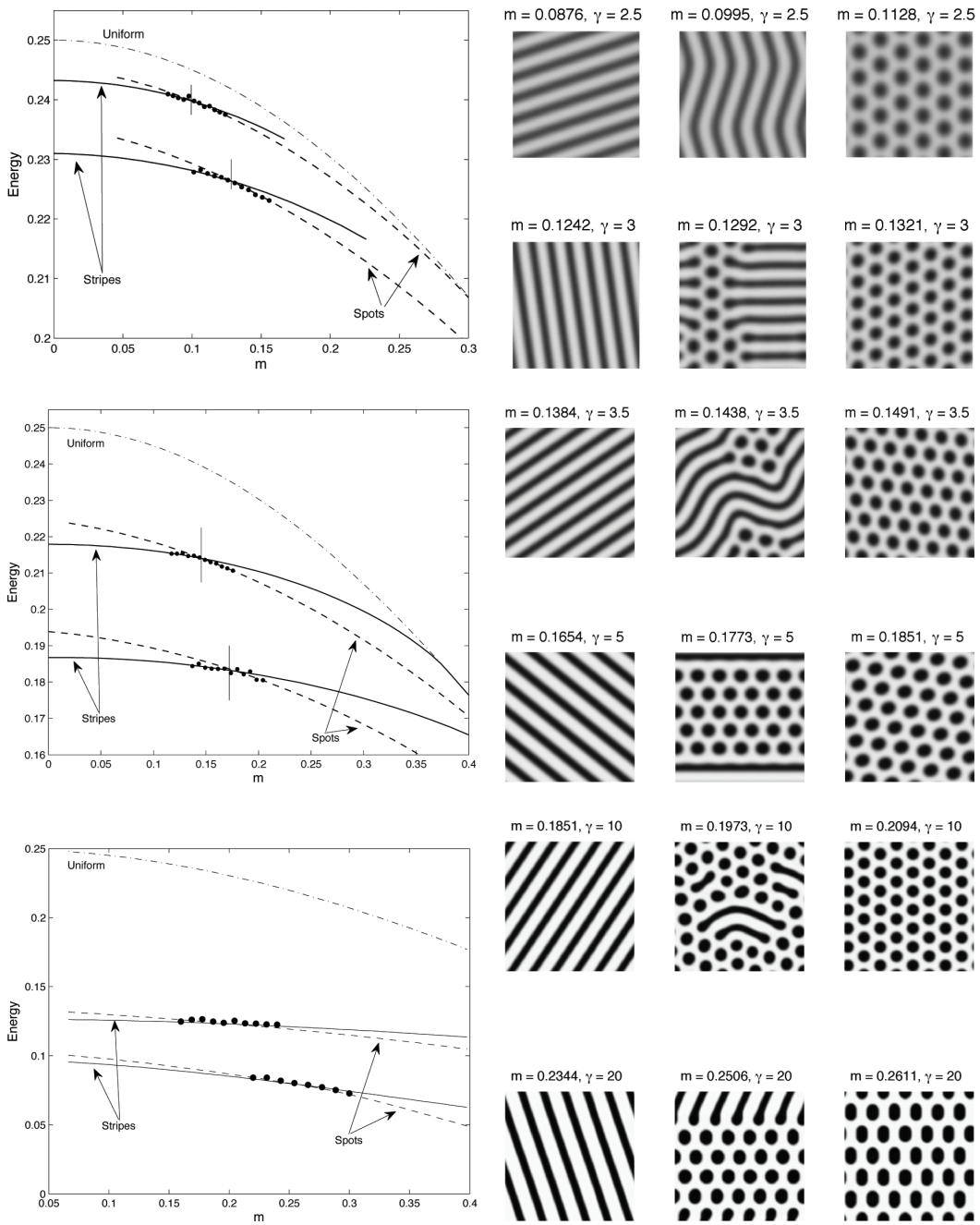


**Figure 5.** *Phase boundaries: Comparison of energies along solution branches for* $\gamma = 2.5, 3, 3.5, 5, 10,$ *and* 20. *Note that the continuation routine failed for some values of* $\gamma$ *on the stripe branch for* $m$ *sufficiently large and on the spot branch for* $m$ *sufficiently small, but these always occurred well beyond the value of* $m$ *at which the branches exchange global stability. In each energy diagram, the lower value of* $\gamma$ *has the higher energy. The vertical bar is the asymptotic value* $m^*(\gamma)$ *where the branches exchange stability. On the right, there are three plots for each run from random initial data:* $m < m^*, m \simeq m^*, m > m^*$. *Here we can see that there is no convergence sufficiently close to* $m^*$ *but that the expected patterns appear away from it.*

based computations is very good. However, computationally continuation is much slower and is not completely reliable. Continuation keeps the geometry fixed as $m$ varies, not necessarily guaranteeing a global minimizer over the whole of the branch. Typically, we computed three branches of solutions and kept the ones with lowest energy in the region of the transition.

**4. Numerical methods.** The details of many aspects of our numerical implementation are straightforward and well understood. We use a pseudospectral method in space, because of the large scale periodicity, and two different time-stepping schemes for evolution. For early times, we use exponential time-differencing (ETD), as the dynamics are quick and we need small time steps to resolve them. ETD provides a cheap per step highly accurate method with well-known stability and accuracy properties for stiff diagonalizable PDEs. For later times we switch to an iterative linearly implicit gradient stable algorithm [43]. This method is more expensive per step and only first-order accurate, but it allows arbitrarily large time steps and guarantees that the energy will not increase.

For all computations we used $N = 256$ spatial modes in both dimensions and $\Delta t = \frac{.1}{1+\gamma^{3/2}}$. The initial choice of domain size was somewhat arbitrary (cf. (4.1)). As we have mentioned the domain size used is sufficiently large with respect to the intrinsic period scale which is determined by $\gamma$. However, even with such a choice, the exact size of the domain can influence both the minimizing patterns and certainly the gradient flow route towards them. Thus we have accounted for this in our algorithm via a *variation of domain size*. This is discussed in section 4.4. Typically we computed for $0 \leq t \leq 100 = t_F$ but took $t_F$ as large as 2500 in some cases. All computations were done on a laptop and implemented in MATLAB. Unless otherwise indicated, the norm of the residual ($||u_t||_2$) is less than $10^{-8}$ in all figures.

**4.1. Metastability.** Figure 6 shows snapshots of a typical run as well as the energy decay over time. Notice that the "final" profile is a labyrinthine pattern rather than pure lamellae or spots but that the energy decay is relatively small at that time. Indeed, Figure 7 shows two quite different configurations whose energies are relatively very close. This phenomenon is pervasive for this problem, as the functional (1.1) has many local minimizers and metastable states near which the dynamics are very slow. Numerically, one cannot distinguish a metastable state from a stable one, since they are both identified as solutions for which the relative change in $\bar{u}$ or $E$ between time steps is smaller than some tolerance level. Furthermore, irregular long lasting states are common in diblock copolymer experiments [16], so, without additional analysis, it is unclear whether they are steady states, rather than just persistent intermediate profiles. Long-lived transient behavior due to the metastability of the Cahn–Hilliard equation is well known (see, for example, [39]), and the metastability is also observed in SCFT numerical calculations [16]. Given that our PDE differs from the Cahn–Hilliard equation only in the extra term (associated with long-range interactions), and can be connected to the SCFT theory (albeit, via further approximations), there is little reason to believe that it can escape the issue of metastability in general. Hence, we need to modify the gradient descent to better approximate the true global minimizers.

**4.2. Selecting and damping modes.** Techniques for dealing with metastability and highly nonconvex energy landscapes often belong to the broad class of statistical methods, called simulated annealing. They were created to navigate through a complex energy landscape in search

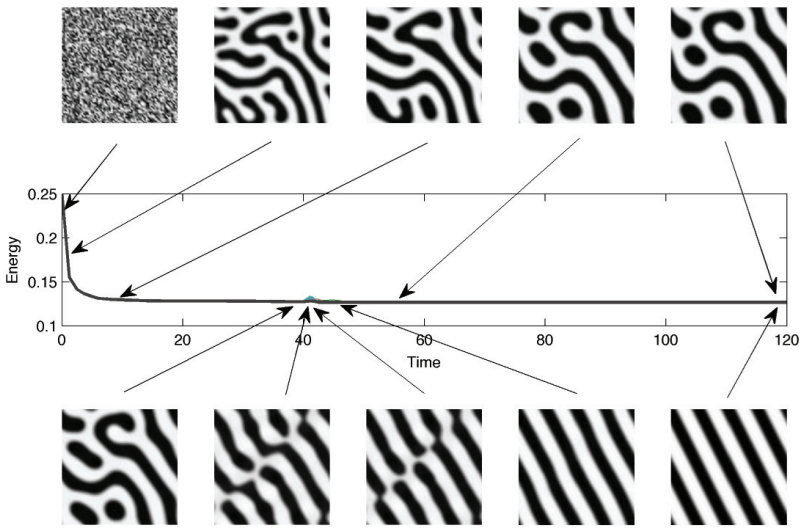


**Figure 6.** *Comparison of two runs with the same initial conditions. The top simply integrates the PDE while the bottom implements the spectral weighting algorithm described in the text. Both runs are identical for* $0 \le t < 40$. *At* $t = 40$ *the spectral weighting is turned on and acts very quickly to allow lamellae to develop. Note that at this scale the difference in the energies is not noticeable (see Figure 8). In both runs* $\gamma = 10$ *and* $m = 0.1$.

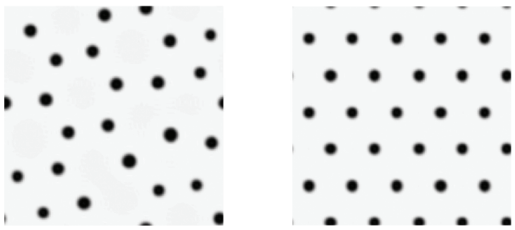

**Figure 7.** *Metastable state with* $\gamma = 20, m = 0.8$. *Left:* $t = 100$. *Right:* $t = 10000$. *The difference in energies between these profiles is less than* $1e-7$, *but clearly the left state is not an energy minimizer, as the packing of spots is irregular. The dynamics are driven by weak interaction between the spots.*

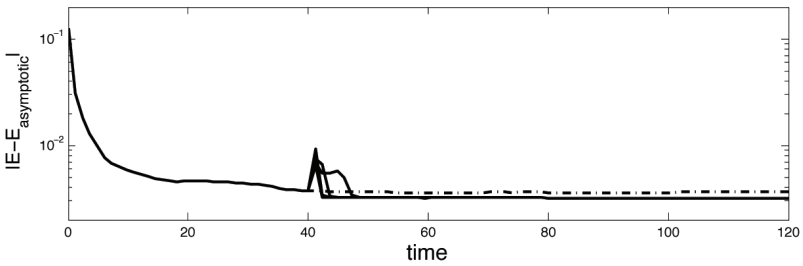


**Figure 8.** *Detail of energy over time for Figure 6. The dashed line has no spectral weighting. The solid lines all have spectral weighting for* $40 < t < 80$. *The damping parameter* $\rho$ *takes the values* $.05, .1, .15, .2, .25,$ *and* $.3$. *Over this range there is no discernible difference in the final states with weighting. For all runs* $\gamma = 10$ *and* $m = 0.1$.

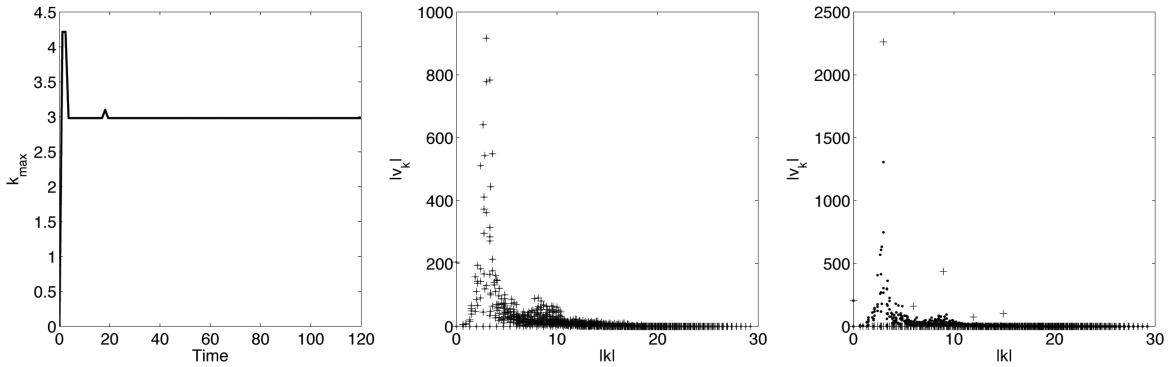


**Figure 9.** *(Left) $k^*$ over time. Here we see that the evolution quickly converges to a dominant length scale and that the spectral weighting does not change it. (Middle) Before the application of the spectral weight most energy is concentrated near the dominant mode $k^*$. (Right) The effect of the spectral weight is to allow the energy to concentrate even more on $k^*$ and its integer multiples.*

of a global minimizer. A very simple form of simulated annealing can be achieved by adding unbiased noise to the evolved metastable state. This may force the solution out of the local minimizer that it is stuck in and make it continue its evolution through the energy landscape. Unfortunately, this approach does not provide a guaranteed way of addressing metastability, as too much noise leads to the divergence of the solution, and even when the solution remains bounded, there is no way of ensuring that it will not revisit the local minimizers that it was stuck in before. Also, the added noise is very quickly damped out due to the fourth-order derivative term in this problem.

A different approach to the removal of defects is provided by the technique of spectral filtering. The essence of this method lies in the removal of insignificant spectral components from an evolved state. That is, we evolve the solution from random initial conditions until a structure is formed, compute its Fourier coefficients, and keep only the modes which correspond to the coefficients above a certain threshold. The evolution is then continued and the process of spectral filtering repeated. This approach was suggested in [16] and, combined with adding noise, applied to our PDE in the following modified form.

Functional (1.1) can be thought of as a length selection mechanism, and, in fact, if we plot the energy concentration in Fourier space over time, we see that this happens quite quickly. Figure 9(left) shows $\hat{v}(k^*, t)$ such that $\max_k \hat{v}(k,t) = \hat{v}(k^*,t)$. In Figure 9(center) we see that the energy is concentrated in a narrow band about $k^*$ in Fourier space. Motivated by this observation we evolve the original PDE until past the point that the dominant length scale has emerged. Denoting this length scale $k^*$ we damp the Fourier coefficients as follows: $\hat{v}(k) \to w(k;k^*)\hat{v}(k)$, where

$$w(k;k^*) = (1-\rho) + \rho\big(\exp\left(-5(1-|k|/k^*)^2\right) + \exp\left(-5(2-|k|/k^*)^2\right) + \exp\left(-5(3-|k|/k^*)^2\right)\big).$$

This keeps information at all wavelengths but focuses the dynamics at the key length scale and its higher harmonics. Experimentation with the parameter $\rho$ indicates that there is little difference in the outcome with $0.05 \le \rho \le 0.3$ as indicated in Figure 8. With $\rho$ too small,

there is no effect and the wrong pattern may emerge if $\rho$ is too large or the standard gradient flow is not run long enough.

This approach allows us to first identify the energy minimizing length scale and the dynamics to focus on these wavelengths, to ensure the local stability of profile which emerged, and then finally to smooth out the effects of added noise. Figure 6 shows two runs from the same initial conditions. The top has no spectral damping and ends up stuck in a metastable state, whereas the bottom leads to the global minimizer. The energy of both runs is shown in Figure 6(middle) where the difference between the two runs is almost indistinguishable. A detailed view of the energy is presented in Figure 8. Lastly, Figure 9(right) shows the coefficient distributions of the final time profiles in Figure 6 with + for the global minimizing state and · for the metastable one. Notice that the spectral weighting did not shift $k^*$ but rather allowed a simpler pattern to emerge.

*Remark.* We have also included four movie files (see 78449_01.mpg [local/web 1.70MB], 78449_02.mpg [local/web 1.73MB], 78449_03.mpg [local/web 1.71MB], and 78449_04.mpg [local/web 1.68MB]) that clearly demonstrate the use of this approach. We compare two cases $(m, \gamma) = (.1, 10)$ and $(m, \gamma) = (.25, 10)$ showing the effect of taking $\rho = 0$ or $\rho = .1$. For $m = .1$, the unmodified run leads to a metastable mixed state including both spots and stripes, whereas the modified run leads to pure stripes with lower energy. For $m = .25$ the unmodified run leads to a nonoptimal collection of spots of differing sizes distributed seemingly randomly. Here, the modified run leads to uniform spots packed on a hexagonal grid. All four runs were started from the same random initial data.

**4.3. Choice of time-stepping method.** When deciding on the most appropriate time discretization scheme for numerical simulations of the PDE, we considered ETD methods of different order and construction as well as two gradient stable schemes based on the work of Eyre [15]. We settled on the ETDRK4 scheme [20], as it has the highest order of accuracy and its stability region is larger than that of the ETD2 scheme. However, the time step is stability limited, so to compute for long times when the dynamics are slow we need something else. For large time steps we found that a fully implicit gradient stable method [15, 43] was the most robust in general and the fastest when we could take large time steps. Combining the two methods led to an algorithm at least 3 times faster than either one alone.

The gradient stable scheme is stable for all time steps[5] and guarantees decay of the energy but requires a nonlinear solve at each time step. The authors in [43] developed an iterative scheme to do this, but the number of iterations required greatly depends on the magnitude of the solution change over each time step. This means it is not feasible to use it to take very large steps at the beginning. To further speed the computation we developed an adaptive time-step routine based on the number of required iterations.

We also considered numerical implementation of the $L^2$ volume constrained gradient flow of the energy functional (1.1). This consideration was motivated by the fact that this evolution system is less stiff than the PDE (1.2), as it contains a Laplacian, rather than a bi-Laplacian term. However, we found that it did not result in a more efficient computation of the steady

[5]In [18], the authors introduce a new interesting unconditionally stable method based on mixed finite elements for space coupled with a second-order accurate time integration. This new method could prove useful for our problem, especially in three dimensions.

states, as it required far more computational steps. This could be because the lower-order derivatives do not damp out high frequency modes as quickly.

Continuation in $m$ was done with a modified Newton method allowing for linearly implicit iterations without computing the $256^2 \times 256^2$ Jacobian matrix.

**4.4. Domain size selection.** We do not know the natural period length of arbitrary solutions, and we do not want to enforce a solution type due to our choice of box size; thus we adaptively choose the domain size. In the limit $\gamma \downarrow 2$ the asymptotic form of the solution has $|k| = \sqrt{2}$, so we take $L_0 = 12\pi$ as a preliminary box size to fit a reasonable number of periods in the box. As $\gamma$ increases, the intrinsic period will decrease. For large $\gamma$, this intrinsic length scales like $(1/\gamma)^{1/3}$ (cf. [29, 8, 36, 1]) and hence as a very rough measure, we found it useful to set the initial domain size as

$$L_\gamma = L_0 \left(\frac{2}{\gamma}\right)^{1/3}. \tag{4.1}$$

However, we want to ensure that we have reached a true global minimizer, and that boundary effects resulting from a "bad" choice of domain size have not prevented us from reaching this goal. Thus at the end of each run, we consider the field $u$ which has been numerically computed on $[0, L]^2$, rescale it to a unit domain $[0, 1]^2$, and examine the rescaled form of the energy per unit area:

$$\begin{aligned}\tilde{E}(L, \tilde{u}, \gamma, m) &= \frac{1}{L^2}\int_{[0,1]^2} \frac{1}{\gamma^2}|\nabla \tilde{u}|^2\, dx + \int_{[0,1]^2} \frac{(1-\tilde{u}^2)^2}{4}\, dx \\ &\quad + L^2 \int_{[0,1]^2}\int_{[0,1]^2} G(x,y)\,(\tilde{u}(x) - m)\,(\tilde{u}(y) - m)\, dx\, dy \\ &=: \frac{1}{L^2\gamma^2} I_1(\tilde{u}) + I_2(\tilde{u}) + L^2 I_3(\tilde{u}, m).\end{aligned}$$

We then minimize $\tilde{E}$ with respect to $L$ for fixed $\tilde{u}$, $\gamma$, and $m$. With this choice of optimal $L$, we then integrate for a small time further to ensure that the energy truly is lower. This also gives us an additional mechanism to find metastable states, as they will have either a higher energy per unit area or an optimal box size drastically different from their near neighbors in the $(m, \gamma)$ plane.

**4.5. Automatic pattern identification.** To aid in the automatic classification of evolved states we examine the distribution of peaks with similar wave length to that of the dominant mode. In particular, we define and analyze the following function:

$$g(\theta) = \int \exp - \frac{|(k_x, k_y) - (\sin\theta, \cos\theta)k^*|^2}{\varepsilon} \hat{v}(k)\, dk.$$

If $g(\theta)$ (where $\theta = \tan^{-1}\frac{k_x}{k_y}$ is the polar angle) is found to have two dominant peaks for $0 \le \theta < 2\pi$, the state is classified as a stripe. If it has six, then it is classified as a hexagonally packed circular state. By symmetry, these are the $n = 1$ (lamellae) and 3 (hexagonally packed spots) cases from section 2, respectively. Labyrinthine structures do not display either of these patterns. This method is not perfect, working only in about 95% of cases.

**4.6. Summary of algorithm.** In summary, we integrate (1.2) using the following algorithm:

1. Set $L = (\frac{2}{\gamma})^{1/3} 12\pi$.
2. Choose random initial data for $\bar{u}$ in $[-1-m, 1-m]$ with mean $m$.
3. Integrate (1.2) using ETDRK4 until $t = t_1$.
4. Integrate (1.2) using ETDRK4 with spectral weighting for $t_1 < t < t_2$.
5. Integrate (1.2) using ETDRK4 with added white noise for $t_2 < t < t_3$.
6. Integrate (1.2) using the nonlinear gradient stable scheme for $t_3 < t < t_4$.
7. Domain size variation/selection of section 4.4.
8. Integrate (1.2) using the nonlinear gradient stable scheme for $t_4 < t < t_5$.
9. Classify the final state.

This procedure may appear overly complicated, but recall that we are attempting to minimize a nonconvex, nonlocal energy in a manner which does not use an anticipated solution structure (as this is not possible in three dimensions), and in a way which is efficient, reliable, and automatic. To do this we have combined two different time-stepping strategies with two different annealing mechanisms.

**5. Unusual agreement with asymptotic analysis.** The calculations of the global stability curves of section 2 give surprisingly good agreement with the results of our spectrally weighted numerical algorithm for a larger range of $\gamma$ than might be initially expected. This agreement extends far beyond the immediate neighborhood of the order-disorder curve. Naturally, this should raise a certain amount of skepticism and concern that the weighted numerical method biases the solutions towards the linear dynamics. Let us address these concerns. First, we note that the spectral weighting is employed for only part of a run. For those parts, it is certainly possible that a certain bias is introduced towards the linear dynamics. However, recall that our fundamental goal here is the phase diagram of (1.1), that is, in parameter space $\gamma$ vs. $m$, characterizing the geometric morphology of the global minimizer. Even without the spectral weighting, all runs gave final states in which the basic pattern dichotomy (spots vs. stripes) was recognizable. The spectral weighting allowed for final states with *lower energy* and which were identical to the *desired* morphology (e.g., straight stripes vs. corrugated). At certain stages of the evolution, it certainly biases the evolution, but this bias enables us to access states of lower energy. Hence if this bias favors the "linear regime" of (1.2), so be it. In fact, all of these conclusions lead to the following observation: For the purposes of describing the basic geometric morphology of the ground state of (1.1), the linear behavior of (1.2) gives very accurate predictions in a (finite) neighborhood of the ODT. This is particularly true for initial data which is a small perturbation of the homogeneous state. That is, the dynamics are initially driven by the linear terms and then there is a large energy barrier to overcome to transition from one phase to the other. In fact, starting with small initial data gives convergence to states as predicted by the asymptotics for $\gamma$ as large as 25. Starting with initial conditions with *large random deviations* generates the diagram presented here, as it is with these less biased initial conditions that we our able to access the lowest energy configurations. The domination of the linear terms in constructing stationary solutions to higher-order PDEs is well known in the folklore but little studied beyond formal observations [6].

**Table 1**

*Variations about the mean as $m^*$ varies along the energy minimizing branches (see Figure 5).*

| $\gamma$ | $m^*$ | $\frac{\text{mean}_m(\max(u)-\min(u))}{2}$ |
|---|---|---|
| 2.001 | 0.0050 | 0.013 |
| 2.01 | 0.0157 | 0.043 |
| 2.1 | .0485 | 0.109 |
| 2.25 | 0.0741 | 0.163 |
| 2.5 | 0.2582 | 0.240 |
| 3 | 0.3333 | 0.317 |
| 3.5 | 0.3780 | 0.413 |
| 5 | 0.4472 | 0.626 |
| 10 | 0.5164 | 0.956 |
| 20 | 0.5477 | 1.021 |

**Figure 10.** *Unusual solutions not predicted by linear analysis. Both these cases have energy lower than the mixed state but are not predicted by the linear analysis.*

However, there is another more fundamental reason why this problem is unusual: The energy has a term which keeps solutions in the linear regime. Solutions to the standard Cahn–Hilliard equation immediately tend to values of $\pm 1 + \mathcal{O}(\varepsilon)$, where $\varepsilon$ is the interfacial thickness. In (1.1), the long-range interactions prefer to keep solutions close to oscillations about the mean. But this is precisely the asymptotic ansatz, and thus it is no surprise that it does well capturing the solutions when they are still in this regime. Table 1 presents the magnitude of fluctuation about the mean as $\gamma$ varies and shows there is a large range of $\gamma$ where the solution is in the asymptotic regime.

There is also a region of the phase diagram where the agreement is quite poor: for large $\gamma$ and large $m$ there is a region where there are very well separated hexagonally packed spots and a very small region where there are Cartesian packed spots as well. Examples of both of these with $\gamma = 20$ are presented in Figure 10. Neither of these behaviors appears for small $m^*$, and the Cartesian packed spots are predicted to never be local minimizers. However, the SCFT does predict a region of "close-packed" spheres which would be the 3D analogue of this behavior.

**6. The outlook for three dimensions.** The 3D problem is considerably more complicated because of the multitude of both local and global minimizers, and, in particular, asymptotic analysis about the ODT curve is far richer due to the larger class of possible symmetries.

Calculations for double gyroid and perforated lamellar symmetries are more complicated but still tractable. Preliminary calculations suggest that these structures can indeed be predicted with an analogous asymptotic analysis about the ODT. Given that phase boundaries will be much more difficult to capture numerically, it is encouraging that at least in two dimensions, asymptotic analysis predicts well these boundaries in a finite neighborhood of the ODT.

In terms of numerics, preliminary experiments suggest that our numerical method is reasonably successful throughout much of the phase plane. As we saw in [10] (though the sample simulations there were performed with a simpler numerical method), metastability issues in three dimensions are even more complex and additional methods of *simulated annealing* may invariably be needed for a full phase diagram close to the ODT. Moreover our blind test for characterization of section 4.5 will need to be augmented with topological calculations on the phase boundary, e.g., the Euler characteristic, as was carried out in the recent work of Teramoto and Nishiura [42].

**Appendix A. Details of the asymptotic calculations.** Recall the linearization of (1.2) about $\bar{u} \equiv 0$:

$$v_t = \mathcal{L}v \equiv -\frac{1}{\gamma^2}\Delta^2 v - (1-3m^2)\Delta v - v,$$

where $v$ is periodic on $[-L_x/2, L_x/2] \times [-L_y/2, L_y/2]$. Taking the Fourier transform shows that the eigenvalues of $\mathcal{L}$ are given by

$$\lambda = -\frac{1}{\gamma^2}|(k_x, k_y)|^4 + (1-3m^2)|(k_x, k_y)|^2 - 1,$$

where $(k_x, k_y)$ represents the 2D wavevector. The condition $\max(\mathrm{Re}(\lambda)) = 0$ determines the ODT curve as

$$\gamma^* = \frac{2}{1-3m^2} \qquad \text{or} \qquad m^* = \sqrt{\frac{\gamma-2}{3\gamma}}.$$

On the ODT curve there is a finite-dimensional center manifold on which we will construct solutions and determine their stability. For $\beta > 0$, we set $m = \beta m^*(\gamma)$ and introduce a regular asymptotic expansion for $\bar{u}$ for small $m^*$:

$$\bar{u}(x,y) \sim m^* \bar{u}_1(x,y) + (m^*)^2 \bar{u}_2(x,y) + \cdots, \tag{A.1}$$

where $\bar{u}_1 \neq 0$, since we are interested in the nonzero solutions of (1.2). Consideration of the $\mathcal{O}(m^*)$ equation along with periodic boundary conditions leads to the following leading-order representation of $\bar{u}$ for $m^* \ll 1$:

$$\bar{u}(x,y,t) \sim m^*\big(a(t)\phi_1(x,y) + b(t)\phi_2(x,y) + c(t)\phi_3(x,y)\big), \tag{A.2}$$

where

$$\phi_1 = \sqrt{2}\cos\Big(\sqrt{2}x\Big), \quad \phi_2 = \sqrt{2}\cos\left(-\frac{1}{\sqrt{2}}x + \sqrt{\frac{3}{2}}y\right), \quad \phi_3 = \sqrt{2}\cos\left(-\frac{1}{\sqrt{2}}x - \sqrt{\frac{3}{2}}y\right).$$

This expansion captures all the possible symmetric periodic configurations described above. Note that these forms are well known in the literature and, since they are enforced by symmetry, quite ubiquitous (see, for example, [26]). We proceed to determine the amplitude

dynamics on the center manifold of (2.1) $X^c = \text{span}\{\phi_1, \phi_2, \phi_3\}$ by projecting the full PDE (1.2) onto $X^c$. Thus, we consider

$$\left\langle \bar{u}_t + \frac{1}{\gamma^2}\triangle^2\bar{u} - \triangle\left(\bar{u}^3 + 3\beta m\bar{u}^2\right) + (1 - 3\beta^2 m^2)\triangle\bar{u} + \bar{u}, \phi_i \right\rangle = 0,$$

for $i = 1, 2, 3$ on the domain $\Omega$, appropriately defined by $L_x = \frac{n\pi}{\sqrt{2}}$ and $L_y = \frac{2}{\sqrt{3}}L_x$. Computing the inner products in $L^2$ and expanding in powers of $m^*$ with the aid of Maple, we find the following amplitude ODE system:

$$\begin{aligned} \dot{a} &= 6(1-\beta^2)a - 6\sqrt{2}\beta bc - 6(b^2+c^2)a - 3a^3, \\ \dot{b} &= 6(1-\beta^2)b - 6\sqrt{2}\beta ac - 6(a^2+c^2)b - 3b^3, \\ \dot{c} &= 6(1-\beta^2)c - 6\sqrt{2}\beta ab - 6(a^2+b^2)c - 3c^3, \end{aligned} \tag{A.3}$$

where time has been rescaled with $(m^*)^2$.

The original equation is a gradient system, and thus the reduced system is one as well. The corresponding Lyapunov function is given by

$$\begin{aligned} V(a,b,c) = &-3(1-\beta^2)(a^2+b^2+c^2) \ + \ 6\sqrt{2}\beta abc \\ &+ 3(a^2b^2+b^2c^2+a^2c^2) \ + \ \frac{3}{4}(a^4+b^4+c^4). \end{aligned} \tag{A.4}$$

This function is in fact the projection of the energy functional (1.1) onto the center manifold $X^c$. We consider the structure and stability of the stationary solutions of the amplitude ODE system by analyzing its Lyapunov function. The stationary states satisfy the following system:

$$V_a(a,b,c) = 0, \ V_b(a,b,c) = 0, \ \text{and } V_c(a,b,c) = 0, \tag{A.5}$$

and they are linearly stable when all eigenvalues of the Hessian matrix, $H(V(a,b,c))$, are positive. We identify five fixed points of the system (A.5):

1. $a = 0$, $b = 0$, $c = 0 \to$ *disorder;*
2. $a = \pm\sqrt{2(1-\beta^2)}$, $b = 0$, $c = 0 \to$ *lamellae;*
3. $a = b = \pm\sqrt{\frac{2(1-\beta^2)}{3}}$, $c = 0 \to$ *rectangular "spots";*
4. $a = \bar{a}$, $b = c = \pm\bar{a}$, where $\bar{a} = -\frac{\sqrt{2}}{5}[\beta \pm \sqrt{5-4\beta^2}] \to$ *hexagonally packed circular spots;*
5. $a = b = \pm\bar{a}$, $c = -\bar{c}$, or $a = -b = \pm\bar{a}$, $c = \bar{c}$, where $\bar{a} = \sqrt{\frac{2(1-5\beta^2)}{3}}$ and $\bar{c} = 2\sqrt{2}\beta \to |a| = b \neq c$ *case.*

While other similar systems can generate other patterns (cf. [19]), none of these appears in this system. We determine the linear stable states and regions (2.2) by evaluating the eigenvalues of $H(V(a,b,c))$ at the five fixed points. We determine (2.3) by evaluating the Lyapunov function at the three linearly stable steady states.

**Acknowledgments.** We would like to thank one of the anonymous referees for his/her questions and many suggestions which significantly improved the article. A preliminary version of this work was contained in the MSc thesis of Mirjana Maras at Simon Fraser University [22].

## REFERENCES


[1] G. Alberti, R. Choksi, and F. Otto, *Uniform energy distribution for minimizers of an isoperimetric problem with long-range interactions*, J. Amer. Math. Soc., 22 (2009), pp. 569–605.

[2] M. Bahiana and Y. Oono, *Cell dynamical system approach to block copolymers*, Phys. Rev. A, 41 (1990), pp. 6763–6771.

[3] F.S. Bates and G.H. Fredrickson, *Block copolymers - Designer soft materials*, Phys. Today, 52 (1999), pp. 32–38.

[4] J. Burke and E. Knobloch, *Localized states in the generalized Swift-Hohenberg equation*, Phys. Rev. E., 73 (2006), 056211.

[5] J.W. Cahn and J.E. Hilliard, *Free energy of a nonuniform system* I. *Interfacial free energy*, J. Chem. Phys., 28 (1958), pp. 258–267.

[6] J.V. Chaparova, L.A. Peletier, and S. Tersian, *Existence and nonexistence of nontrivial solutions of fourth- and sixth-order ordinary differential equations*, Adv. Differential Equations, 8 (2003), pp. 1237–1258.

[7] X. Chen and Y. Oshita, *An application of the modular function in nonlocal variational problems*, Arch. Ration. Mech. Anal., 186 (2007), pp. 109–132.

[8] R. Choksi, *Scaling laws in microphase separation of diblock copolymers*, J. Nonlinear Sci., 11 (2001), pp. 223–236.

[9] R. Choksi and M.A. Peletier, *Small volume-fraction limit of the diblock copolymer problem:* II. *Diffuse-interface functional*, SIAM J. Math Anal., 43 (2011), pp. 739–763.

[10] R. Choksi, M.A. Peletier, and J.F. Williams, *On the phase diagram for microphase separation of diblock copolymers: An approach via a nonlocal Cahn–Hilliard functional*, SIAM J. Appl. Math., 69 (2009), pp. 1712–1738.

[11] R. Choksi and X. Ren, *On a derivation of a density functional theory for microphase separation of diblock copolymers*, J. Statist. Phys., 113 (2003), pp. 151–176.

[12] R. Choksi and P. Sternberg, *On the first and second variations of a nonlocal isoperimetric problem*, J. Reine Angew. Math., 611 (2007), pp. 75–108.

[13] M.C. Cross and P.C. Hohenberg, *Pattern formation outside of equilibrium*, Rev. Modern Phys., 65 (1993), pp. 851–1111.

[14] K.R. Elder, M. Katakowski, M. Haataja, and M. Grant, *Modeling elasticity in crystal growth*, Phys. Rev. Lett., 88 (2002), 245701.

[15] D. Eyre, *An unconditionally stable one-step scheme for gradient systems*, unpublished paper, 1998; available online from http://www.math.utah.edu/ eyre/research/methods/stable.ps.

[16] G.H. Fredrickson, *The Equilibrium Theory of Inhomogeneous Polymers*, Oxford Science Publications, Clarendon Press, Oxford, UK, 2006.

[17] A.K. Khandpur, S. Förster, F.S. Bates, I.W. Hamley, A.J. Ryan, W. Bras, K. Almdal, and K. Mortensen, *Polyisoprene-polystyrene diblock copolymer phase diagram near the order-disorder transition*, Macromolecules, 28 (1995), pp. 8796–8806.

[18] H. Gomez and T.J.R. Hughes, *Provably unconditionally stable, second-order time-accurate, mixed variational methods for phase-field models*, J. Comput. Phys., 230 (2011), pp. 5310–5327.

[19] R. Hoyle, *Pattern Formation: An Introduction to Methods*, Cambridge University Press, Cambridge, UK, 2006.

[20] A.-K. Kassam and L.N. Trefethen, *Fourth-order time-stepping for stiff PDEs*, SIAM J. Sci. Comput., 26 (2005), pp. 1214–1233.

[21] D.J.B. Lloyd, B. Sandstede, D. Avitabile, and A. R. Champneys, *Localized hexagon patterns of the planar Swift–Hohenberg equation*, SIAM J. Appl. Dyn. Syst., 7 (2008), pp. 1049–1100.

[22] M. Maras, *The 2D Phase Diagram Associated with a PDE Model for Self-Assembly of Diblock Copolymers*, MSc thesis, Simon Fraser University, Burnaby, BC, Canada, 2009.

[23] M.W. Matsen and M. Schick, *Stable and unstable phases of a diblock copolymer melt*, Phys. Rev. Lett., 72 (1994), pp. 2660–2663.

[24] C.B. Muratov, *Theory of domain patterns in systems with long-range interactions of Coulomb type*, Phys. Rev. E., 66 (2002), 066108.

[25] C.B. Muratov, *Droplet phases in non-local Ginzburg-Landau models with Coulomb repulsion in two dimensions*, Comm. Math. Phys., 299 (2010), pp. 45–87.
[26] J.D. Murray, *Mathematical Biology* II: *Spatial Models and Biomedical Applications*, 3rd ed., Springer, Berlin, 2003.
[27] Y. Nishiura, *Far-From Equilibrium Dynamics*, Trans. Math. Monogr. 209, AMS, Providence, RI, 2002.
[28] Y. Nishiura and I. Ohnishi, *Some mathematical aspects of the micro-phase separation in diblock copolymers*, Phys. D, 84 (1995), pp. 31–39.
[29] T. Ohta and K. Kawasaki, *Equilibrium morphology of block copolymer melts*, Macromolecules, 19 (1986), pp. 2621–2632.
[30] L.A. Peletier and W.C. Troy, *Spatial Patterns: Higher Order Models in Physics and Mechanics*, Progr. Nonlinear Differential Equations Appl. 45, Birkhäuser Boston, Boston, MA, 2001.
[31] L.A. Peletier and J.F. Williams, *Some canonical bifurcations in the Swift–Hohenberg equation*, SIAM J. Appl. Dyn. Syst., 6 (2007), pp. 208–235.
[32] S. Puri and H.L. Frisch, *Segregation dynamics of binary mixtures with simple chemical reactions*, J. Phys. A, 27 (1994), pp. 6027–6038.
[33] X. Ren and J. Wei, *On energy minimizers of the diblock copolymer problem*, Interfaces Free Bound., 5 (2003), pp. 193–238.
[34] X. Ren and J. Wei, *Wriggled lamellar solutions and their stability in the diblock copolymer problem*, SIAM J. Math. Anal., 37 (2005), pp. 455–489.
[35] C. Sagui and R.C. Desai, *Kinetics of phase separation in two-dimensional systems with competing interactions*, Phys. Rev. E, 49 (1994), pp. 2225–2244.
[36] E.N. Spadaro, *Uniform energy and density distribution: Diblock copolymer functional*, Interfaces Free Bound., 11 (2009), pp. 447–474.
[37] K. Staliunas and V.J. Sanchez-Morcillo, *Dynamics of phase domains in the Swift-Hohenberg equation*, Phys. Lett. A, 241 (1998), pp. 28–34.
[38] P. Sternberg and I. Topaloglu, *On the global minimizers of a nonlocal isoperimetric problem in two dimensions*, Interfaces Free Bound., 13 (2011), pp. 155–169.
[39] X. Sun and M.J. Ward, *Dynamics and coarsening of interfaces for the viscous Cahn-Hilliard equation in one spatial dimension*, Stud. Appl. Math., 105 (2000), pp. 203–234.
[40] J. Swift and P.C. Hohenberg, *Hydrodynamic fluctuations at the convective instability*, Phys. Rev. A, 15 (1977), pp. 319–328.
[41] T. Teramoto and Y. Nishiura, *Double gyroid morphology in a gradient system with nonlocal effects*, J. Phys. Soc. Japan, 71 (2002), pp. 1611–1614.
[42] T. Teramoto and Y. Nishiura, *Morphological characterization of the diblock copolymer problem with topological computation*, Jpn. J. Ind. Appl. Math., 27 (2010), pp. 175–190.
[43] Z. Xu, A. Christlieb, and K. Promislow, *On the unconditionally gradient stable scheme for the Cahn–Hilliard equation and its implementation with Fourier method*, SIAM J. Sci. Comput., submitted.